A combined experimental and theoretical approach revealing a direct mechanism for bifunctional water splitting on doped copper phosphide

Indranil Mondal, *[a] Arup Mahata, *[b,c] Heeyoung Kim,[d] Ujjwal Pal, [e]

Filippo De Angelis, *[b,c,f] and Jeong Y. Park *[a,d]

Author Affiliations:

*Corresponding authors

[a]Center for Nanomaterials and Chemical Reactions, Institute for Basic Science (IBS), Daejeon 34141, Republic of Korea
E-mail: indraiict@gmail.com, jeongypark@kaist.ac.kr

[b]Computational Laboratory for Hybrid/Organic Photovoltaics (CLHYO), Istituto CNR di Scienze e Tecnologie Chimiche "Giulio Natta" (CNR-SCITEC), Via Elce di Sotto 8, 06123 Perugia, Italy
E-mail: arup.mahata@iit.it, filippo@thch.unipg.it

[c]CompuNet, Istituto Italiano di Tecnologia, Via Morego 30, 16163 Genova, Italy

[d]Department of Chemistry, Korea Advanced Institute of Science and Technology (KAIST), Daejeon, Republic of Korea

[e]Department of Energy and Environmental Engineering, CSIR-Indian Institute of Chemical Technology, Hyderabad 500007, India

[f]Department of Chemistry, Biology and Biotechnology, University of Perugia, Via Elce di Sotto 8, 06123 Perugia, Italy

Abstract

A cost-effective electrocatalyst should have a high dispersion of active atoms and a controllable surface structure to optimize activity. Additionally, bifunctional characteristics give an added benefit for the overall water splitting. Herein, we report the synthesis and fabrication of Fe-doped Cu/Cu_3P supported on a flexible carbon cloth (CC) with a hydrophilic surface for efficient bifunctional water electrolysis under alkaline conditions. Surface doping of Fe in the hexagonal Cu_3P does not alter the lattice parameters, but it promotes the surface metallicity by stimulating $Cu^{\delta+}$ and Cu^0 sites in Cu_3P, resulting in an augmented electroactive surface area. $Cu_{2.75}Fe_{0.25}P$ composition exhibits unprecedented OER activity with a low overpotential of 470 mV at 100 mA cm^{-2}. Under a two electrode electrolyzer system the oxygen and hydrogen gas was evolved with an unprecedented rate at their respective electrode made of same catalyst. Density functional theory further elucidates the role of the Fe center toward electronic state modulation, which eventually alters the entire adsorption behavior of the reaction intermediates and reduces the overpotential on Fe-doped system over pristine Cu_3P.

1. Introduction

The generation of hydrogen and oxygen *via* water electrolysis is a promising environmentally friendly technique to meet future global terawatt energy demands.[1,2] The oxygen evolution reaction (OER) is both thermodynamically and kinetically challenging, involving four concerted proton-coupled electron transfer steps. In compensating for this difficulty, ruthenium (Ru)/iridium (Ir)-based materials make excellent

catalysts for the OER in both acidic and alkaline solutions.[3,4] The hydrogen evolution reaction (HER) is similarly optimized with Pt-based catalysts, but their high cost and low elemental abundance limit their application in large-scale water splitting. Therefore, it is necessary to develop highly efficient non-noble catalysts for the overall water electrolysis with low overpotential (OP) consumption for large-scale commercialization.

Among the Earth-abundant electrocatalysts, first row 3d metal phosphides have received tremendous attention as HER catalysts due to their optimal binding energy with H in different reaction media, controllable bulk phase and oxidation state of the metal in phosphides, and corrosion resistivity.[5] Since Schaak *et al.* first demonstrated the HER performance of facet-modulated Ni_2P,[6] a variety of transition metal phosphides, such as CoP,[7] Cu_3P,[8,9] Ni_xP_y,[5,10] FeP,[11] and MoP,[12] have been developed as efficient HER catalysts. On the other hand, metal non-oxides such as carbides,[13] chalcogenides (including the biomimetic catalyst),[14–18] nitrides,[19] and phosphides,[20,21] and layered hydroxides[22] have been moderately investigated as an alternative to the conventional metal oxide OER catalysts. However, the role of active species and understanding of the OER mechanism in metal phosphide catalysts remain out of reach, which makes it difficult to modulate the metal phosphide electronically and topologically. It is generally believed that the metalloid nature of transition metal phosphides (TMPs) together with the *in situ* formed metal-oxo/hydroxo species on pre-catalyst surfaces under OER conditions synergistically contribute to the enhanced oxygen evolution by the electrochemical cold working of TMP.[23–25] In many cases, TMPs were even more active than the corresponding oxide/hydroxide catalysts of the same metallic entity.[25,26]

Owing to its outstanding cycling performance and gravimetric specific capacity (363 mA h g^{-1}), binary copper phosphide (Cu_3P) has garnered most of the attention for exhibiting suitable charge–discharge properties in battery applications.[27–29] Moreover, Cu_3P is a metal-rich phosphide and does not suffer from solvent co-intercalation reactions.[30] Cu_3P has also been used in photocatalysis as a heterostructure, either with a metal or with another semiconductor.[31,32] Even though recent studies indicate the potential of Cu_3P as an HER electrocatalyst,[9,33,34] its electronic and surface properties are not sufficiently understood for successful modulation for the bifunctional electrocatalytic reaction.

Herein, we have developed a direct and effective approach to synthesize, for the first time, Fe-doped Cu/Cu_3P *via* a simple hydrothermal reaction, followed by solid-state phosphidation on a 3D carbon cloth for bifunctional water splitting reactions. Fe doping at the surface promotes the formation of highly active metallic Cu^0 nanoparticles. Moreover, the presence of Fe d-state density at the Fermi level dominates the adsorption behavior of reaction intermediates at the Fe sites of Fe-doped Cu_3P system. Such topological and electronic modulation with the doping of 10 mol% Fe results in the reduction of the OER and HER OPs by 240 and 158 mV, as compared to the undoped catalysts at 100 mA cm^{-2}. Finally, the post-*operando* studies clearly reveal the surface active species and the underlying mechanism behind alkaline water electrolysis.

2.1 Structural characterization

The fabrication of flexible Fe-doped Cu/Cu_3P film as a working electrode material is shown in Scheme 1. Cu_3P and Fe-doped Cu_3P were synthesized directly on a thoroughly cleaned carbon cloth substrate *via* thermal phosphidation of the Fe/Cu precursor film. The Fe/Cu precursor is detected as phase pure carbonated $Cu(OH)_2$ (malachite; JCPDS: 01-075-1163) (Fig. S1a†). No peak was detected for an Fe-containing compound. However, a clear Fe^{2+} peak was observed in the XPS of the post-hydrothermal product (Fig. S1b†). The synthesis method is detailed in the Experimental section. The morphology of the precursor and the final composite did not change after phosphidation at 300 °C. Unlike pristine Cu_3P, Fe

doping resulted in nanocucurbit morphology with a roughly spherical shape. The conditions for the thermal phosphidation are identical in all preparations, regardless of the doping percentage. As shown in Fig. S1c,† prior to the phosphidation, both doped and undoped Cu_3P are isolated with a pure hexagonal phase (space group $P6_3cm$, JCPDS: 1-71-2261).[28] The crystal cell parameter indicates a similar crystalline volume of Cu_3P before and after the Fe doping (Table S1†). Importantly, the XRD pattern indicates the presence of metallic fcc Cu peaks appearing at 31°, 43.4° and 50.5° (Fig. S1c†).[28] With an increase in the Fe doping, the relative peak intensity for fcc Cu increased, which means that the Fe center (as Fe^{2+}) may promote the reduction of Cu^{2+} to Cu^0.[35] The occupancy of the Cu^0 phase in $Cu_{2.75}Fe_{0.25}P$ is calculated as 43% using the Rietveld refinement (Table S1†). The hexagonal phase of Cu_3P is clearly retained and no XRD peak shifting occurs after Fe doping. The cell parameters and cell volume of Cu_3P are unaltered after Fe doping. (Table S1†). This is similar to the theoretical observation of Fe-doped Cu_2O crystals, which exhibits a slight change in the relative bond length of Cu–O after Fe doping.[36] No distinct peak was observed for FeP or for any newly formed species. The scanning electron microscopy (SEM) images showed the top view of the Cu_3P dendritic structure (Fig. 1a). The thick Cu_3P wall can be observed in the transmission electron microscopy (TEM) image with a (110) facet exposed on the surface (Fig. 1b). The selected area electron diffraction pattern (SAED) indicated the polycrystalline nature of pristine Cu_3P clearly indexed to the (300) and (222) planes (Fig. 1c).[37] Fe-doped Cu/Cu_3P uniformly covered each fiber of the carbon cloth, and efficiently utilized the surface of the carbon cloth (Fig. 1f). In both doped and undoped Cu_3P, the small-sized Cu nanoparticles (at approximately 2 nm) were visible and flanked on the Cu_3P support. It is worth noting that the Cu nanoparticles flanked onto the catalyst surface were found to be air-stable and unsusceptible to surface oxidation, because it did not show any oxide species on the well-resolved lattice fringes of the Cu (111) plane. The successful doping of Fe was further confirmed by the reduced lattice *d*-spacing of (110) plane of Cu_3P (Fig. S2†). The addition of dopant metals with relatively high redox potentials compared to host metals (here Cu)[38] could promote the electron transfer from the host metal to the dopant and increase the stability of the integrated system. Due to the elevation of the Fe doping, the building blocks of the nanostructure shrink slightly, but maintain their integral structure (Fig. S3†). As a result of this topological change, the surface hydrophilicity increased, as evidenced by the reduced contact angle with increased doping concentration (Fig. 1l). SEM energy dispersive X-ray spectroscopy (EDXS) reveals the presence of copper, iron and phosphorus with the empirical elemental compositions of $Cu_{2.95}Fe_{0.05}P$, $Cu_{2.75}Fe_{0.25}P$ and $Cu_{2.46}Fe_{0.54}P$ for the theoretical 2, 10, and 20 mol% doping of Fe, respectively (Fig. S4†). Furthermore, the inductively coupled plasma atom emission spectrometry (ICP-AES) analysis also closely matched the EDXS results (Table S2†). High-resolution X-ray photoelectron spectra (XPS) showed the surface and sub-surface chemical states of Cu and P before and after doping. Like pristine Cu/Cu_3P, the deconvoluted peaks of Cu $2p_{3/2}$ in the Fe-doped Cu/Cu_3P clearly indicated the presence of $Cu^{\delta+}$ and some Cu^{2+} at 932.40 eV and 934.39 eV, respectively, along with the satellite peak at 943.50 eV (Fig. S5†). Moreover, Fe doping led to a slight negative shift (0.34 eV) in the Cu 2p binding energy, as compared to the undoped Cu_3P, indicating an electronic interaction between Cu and Fe.[26] Fe is probably doped on the surface Cu site of Cu_3P and majorly exposed as Fe^{2+}. The BE values at 709.5 and 710.3 eV obtained from the deconvoluted peak of Fe $2p_{3/2}$ could be associated with Fe^{2+} and Fe^{3+} in $Cu_{2.75}Fe_{0.25}P$ (as a representative catalyst) (Fig. S6†).[39] In P 2p, two peaks at 129.3 and 130.0 eV can be assigned to the M–P bond, while the peak at 134.1 eV reflects the surface oxidized P species, usually arising due to air exposure (Fig. S7†).[39,40]Fig. 2a shows the XPS valence-band spectra on a clean surface of Cu_3P and $Cu_{2.75}Fe_{0.25}P$. The BE energy value for the Cu d-band center is 3.52 eV for Cu/Cu_3P (undoped). However, the value shifted towards higher BE (0.72 eV) after Fe doping. To further confirm, DFT calculations were performed on Cu_3P and Fe-doped Cu_3P bulk lattice using the experimental cell parameters (see the ESI† for computational details). DFT results show the shifting of the d-band center from −3.42 eV for Cu_3P to −3.08 eV for $Cu_{2.75}Fe_{0.25}P$ (Fig. 2b and c). Such d-

band center shifting originates from the d-d hybridization between Cu-d and Fe-d states, as indicated by the density of states plot for the Fe-doped Cu_3P doped system (inset in Fig. 2c). Moreover, the Fe d-state density of the Fe-doped Cu_3P system lies at the Fermi level, which might have a significant influence on the adsorption behavior of the intermediates, and thereby on the reaction OP.

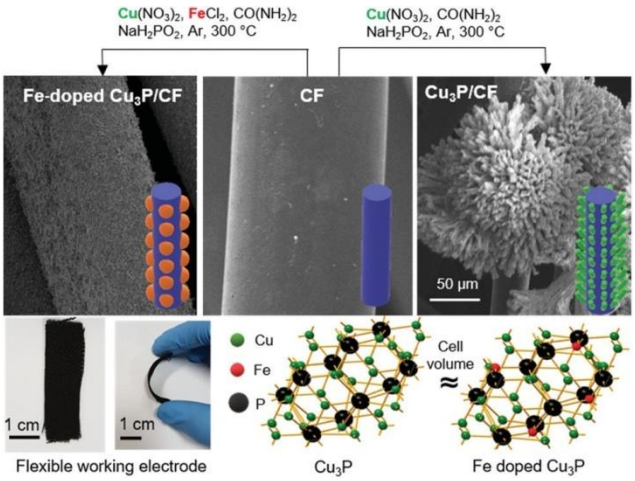

Scheme 1. Fabrication of Cu_3P and Fe-doped Cu_3P grown on a carbon cloth (CC) as flexible electrodes for bifunctional water splitting. The as- prepared Cu_3P and Fe-doped Cu_3P crystallized as the hexagonal phase $P6_3cm$ unit with almost the same cell volume.

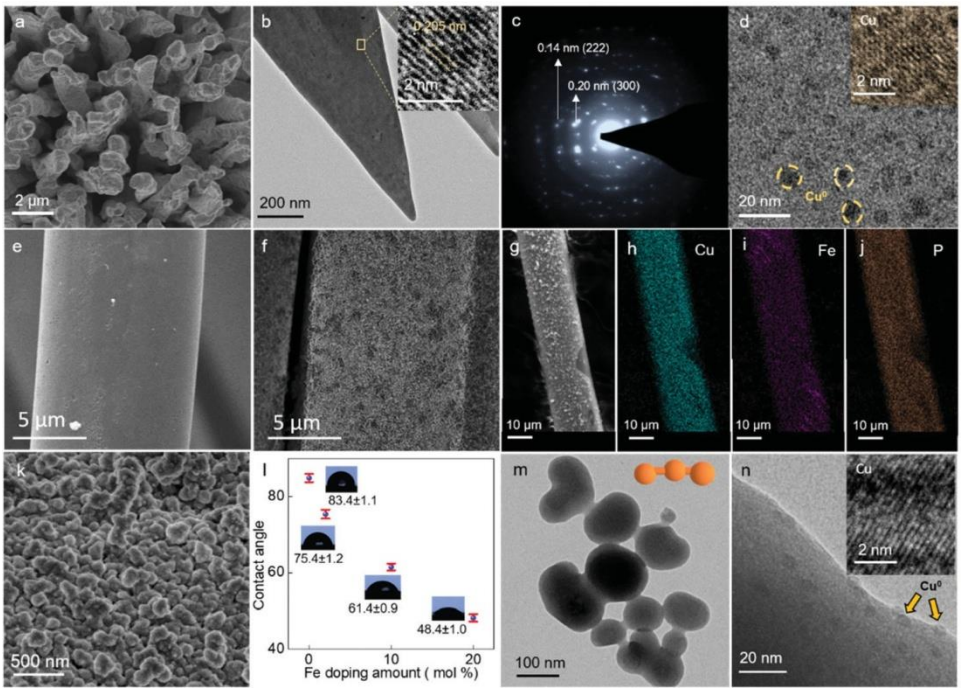

Fig. 1 (a) Top view of the SEM image of pristine Cu_3P dendritic morphology; (b) low magnification TEM and HRTEM (inset) of pristine Cu_3P; (c) TEM SAED pattern extracted from the selected area shown in the inset of Fig. 2b; (d) higher magnification TEM image of Cu_3P surface with ultra-small dis- persed Cu nanoparticles; inset shows the HRTEM image of Cu nanoparticles; SEM image of (e) pure carbon cloth fiber and (f) Fe-doped Cu_3P ($Cu_{2.75}Fe_{0.25}P$) catalyst grown on a carbon cloth; (g–j) SEM EDX elemental mapping of Fe-doped Cu_3P ($Cu_{2.75}Fe_{0.25}P$) grown on a carbon cloth; (k) SEM image of a Fe-doped Cu_3P ($Cu_{2.75}Fe_{0.25}P$) surface; (l) the measured contact angle on different catalyst surfaces grown on a carbon cloth; (m) TEM image of Fe-doped Cu_3P ($Cu_{2.75}Fe_{0.25}P$), which shows the nanocucurbit morphology and (n) the higher magnification TEM image

of Fe-doped Cu_3P ($Cu_{2.75}Fe_{0.25}P$) catalyst surface (inset shows the HRTEM image of Cu nanoparticles observed on the catalyst surface).

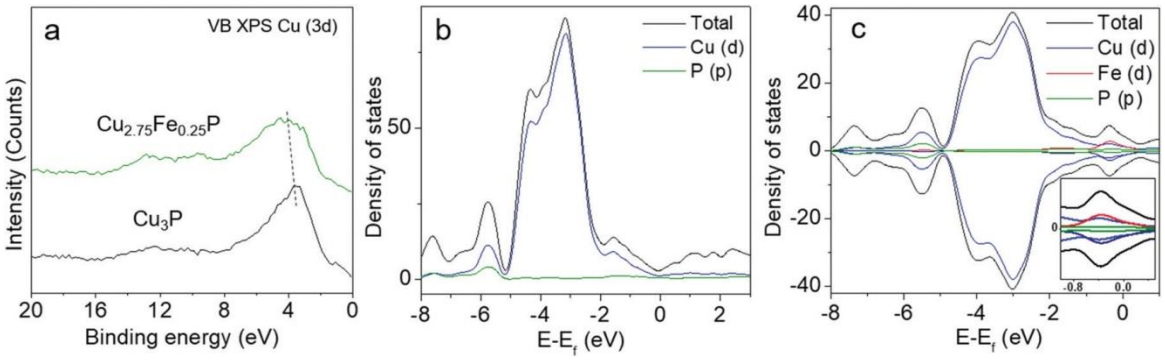

Fig. 2 (a) Cu 3d valence band XPS of Cu_3P and Fe-doped Cu_3P ($Cu_{2.75}Fe_{0.25}P$); DOS plot for (b) pristine Cu_3P and (c) Fe-doped Cu_3P (theoretically one Fe atom doped in the pristine Cu_3P slab).

2.2 Electrochemical behavior

A standard three-electrode configuration was employed to check the water splitting performance of the Fe-doped Cu/Cu_3P catalysts by directly dipping the fabricated electrode in an Ar-saturated 1 M KOH solution. The polarization curves for both HER and OER were recorded at a scan rate of 20 mV s^{-1} (without iR correction). Assessing the OER performances showed that the $Cu_{2.75}Fe_{0.25}P$ catalyst reaches the current density of 100 mA cm^{-2} with an overpotential of 470 mV, which is lower than $Cu_{2.95}Fe_{0.05}P$ (640 mV) and $Cu_{2.46}Fe_{0.54}P$ (550 mV), indicating the optimized concentration for Fe doping for the electronic modulation of Cu_3P (Fig. 3a). The current density value for $Cu_{2.75}Fe_{0.25}P$ and IrO_2 (as control) slightly starts to increase from 0 at approximately 1 V. The Tafel slopes were calculated from the LSV curve (Fig. 3b). The smallest slope value was obtained as 67.5 mV dec^{-1} for $Cu_{2.75}Fe_{0.25}P$, presumably indicating the OER kinetics with four electron transfers and O–O bond formation as rate-determining steps.[41] This is typical of phosphide-based catalysts.[42] The open circuit potential (OCP) value indicates the thermodynamic tendency toward the oxidation of the electrocatalyst surface while scanning from negative to positive potential (Fig. 3c).[43] The oxidized surface could be a passivation layer,[44,45] an intermediate or active electrocatalyst surface generated *in situ* on the pre-catalyst surface.[45,46] The OCP value reduced with increased Fe doping, indicating that more Fe, Cu and P sites were adsorbed by the reaction intermediates and, eventually, was oxidized.

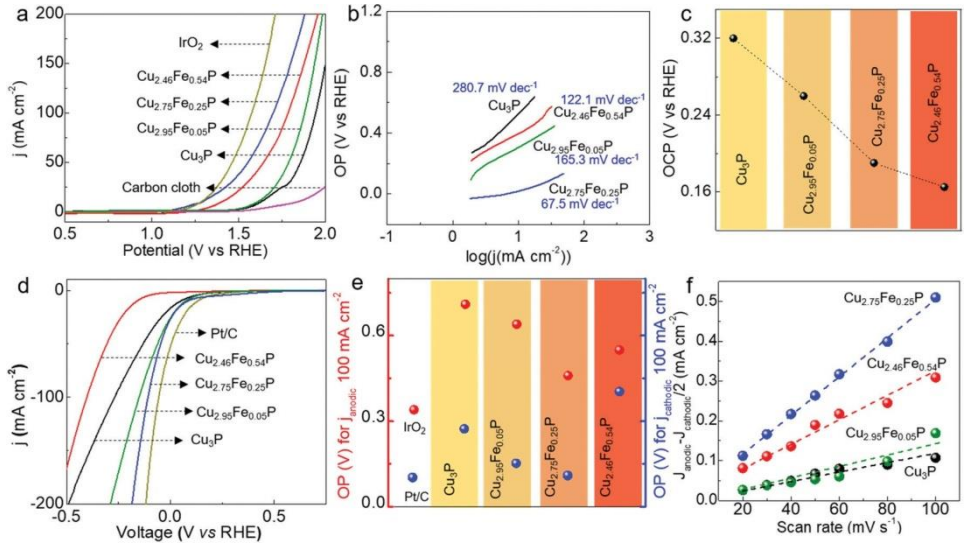

Fig. 3 (a) Anodic polarization curves for the Fe-doped Cu_3P/CC electrode, which are compared with pristine Cu_3P and commercial IrO_2; (b) corres- ponding Tafel plots (c) open circuit potential (OCP) values observed after dipping the electrodes in the electrolyte solution; (d) cathodic polarization curve for various Fe-doped Cu_3P/CC, which are compared with pristine Cu_3P and commercial Pt/C; (e) the calculated overpotentials for the catho- dic and anodic half reactions based on the performance of different Fe-doped Cu_3P catalysts and (f) the capacitive currents at 0.25 V as a function of scan rate for various catalysts deposited on a carbon cloth.

The HER activity of the as-prepared catalysts was investigated under the same experimental conditions as in the OER and compared with Pt/C as the control (Fig. 3d). Like the OER activity, $Cu_{2.75}Fe_{0.25}P$ exhibited remarkable results, even though it required a significant effort to get closer to Pt/C. At the onset potential of HER (0 V *vs.* RHE), $Cu_{2.75}Fe_{0.25}P$ generated 10 mA cm^{-2}, whereas Pt/C generated 45 mA cm^{-2}. $Cu_{2.46}Fe_{0.54}P$ (the highest Fe doping concentration) exhibited poor activity among all the catalysts, because Fe may act as a catalyst poison. With increased Fe doping concentration, the number of metallic Cu nanoparticles gradually increases, which could apparently enhance the HER activity. However, the Cu nanoparticles might not be the only factor. Furthermore, during the HER, no oxide or hydroxide species form, as they do in the OER. Thus, the reason for the drastic change in HER activity remains ambiguous to this point, but will be addressed later. The electrochemically active surface area (ECSA) was measured by extracting the double layer capacitance (C_{dl}) from the cyclic voltammogram under a different scan rate at the non-faradaic potential region (Fig. S8, 3f and detailed discussion in the ESI†). The maximum C_{dl} value obtained with $Cu_{2.75}Fe_{0.25}P$ (5 µF cm^{-2}) implies highly available active sites in the optimized Fe-doped Cu/Cu_3P composite. It is understood from these experimental results that Fe^{2+} site in the Fe-doped Cu/Cu_3P composites reduces the OP by altering the adsorption energies of OER intermediates, but the activity decreases if the catalyst is Fe–rich. This may be due to (i) the formation of FeO_xH_y,[47] or (ii) Fe^{2+}–Fe^{3+} pair-assisted charge transfer, leading to a decrease in the polarity of Cu_3P surfaces.[48] Thus, the role of the active sites turns out to be a critical center of interest, prompting us to focus on the DFT calculations and post *operando* characterization.

DFT calculations have been performed to understand the adsorption behavior of the reaction intermediates and the reaction OP upon Fe substitution by considering the (0001) surface of Cu_3P. The CuP-terminated surface appears to be more stable than the Cu-terminated surface (see Fig. S9, Table S3 in the ESI†). We have considered all the possible sites for the adsorption of OER intermediates. The most preferential binding sites of the intermediates on the surface have been shown in Fig. 4a and b and the corresponding adsorption energies are provided in Table 1, whereas the adsorption energies for all the possible sites are provided in Table S4.† We found that Fe^{2+} is the primary adsorption site for the OER reaction intermediates. In-depth analysis on the bond lengths of the reaction intermediates revealed that the O–O bond distances of adsorbed-OOH are 1.49 and 1.46 Å for Cu_3P and Fe-doped Cu_3P, respectively. Therefore, *OOH in an Fe-doped system is more like O_2 (bond distance, 1.21 Å), favoring the Fe-doped Cu_3P as a better catalyst for the OER. Furthermore, the different adsorption behaviors of the systems also contribute towards the catalytic activity. Here, we have studied all the possible elementary reaction steps of the OER on the surface of Cu_3P and Fe-doped Cu_3P catalyst to calculate the overpotential of the reaction as proposed by Nørskov and co-workers.[49,50] The OER is a four-electron water oxidation reaction and the most probable reaction steps in the alkaline medium are as follows [eqn (1)–(4)]:

$$* + OH^- \rightarrow *OH + e^-, (1)$$

$$*OH + OH^- \rightarrow *O + H_2O(l) + e^-, (2)$$

$$*O + OH^- \rightarrow *OOH + e^-, (3)$$

$$*OOH + OH^- \rightarrow * + O_2(g) + H_2O(l) + e^-, (4)$$

where, an asterisk (*) sign and *X (X = O, OH, and OOH) represent the catalyst surface and the adsorbed oxygenated species on the catalyst surface, respectively.

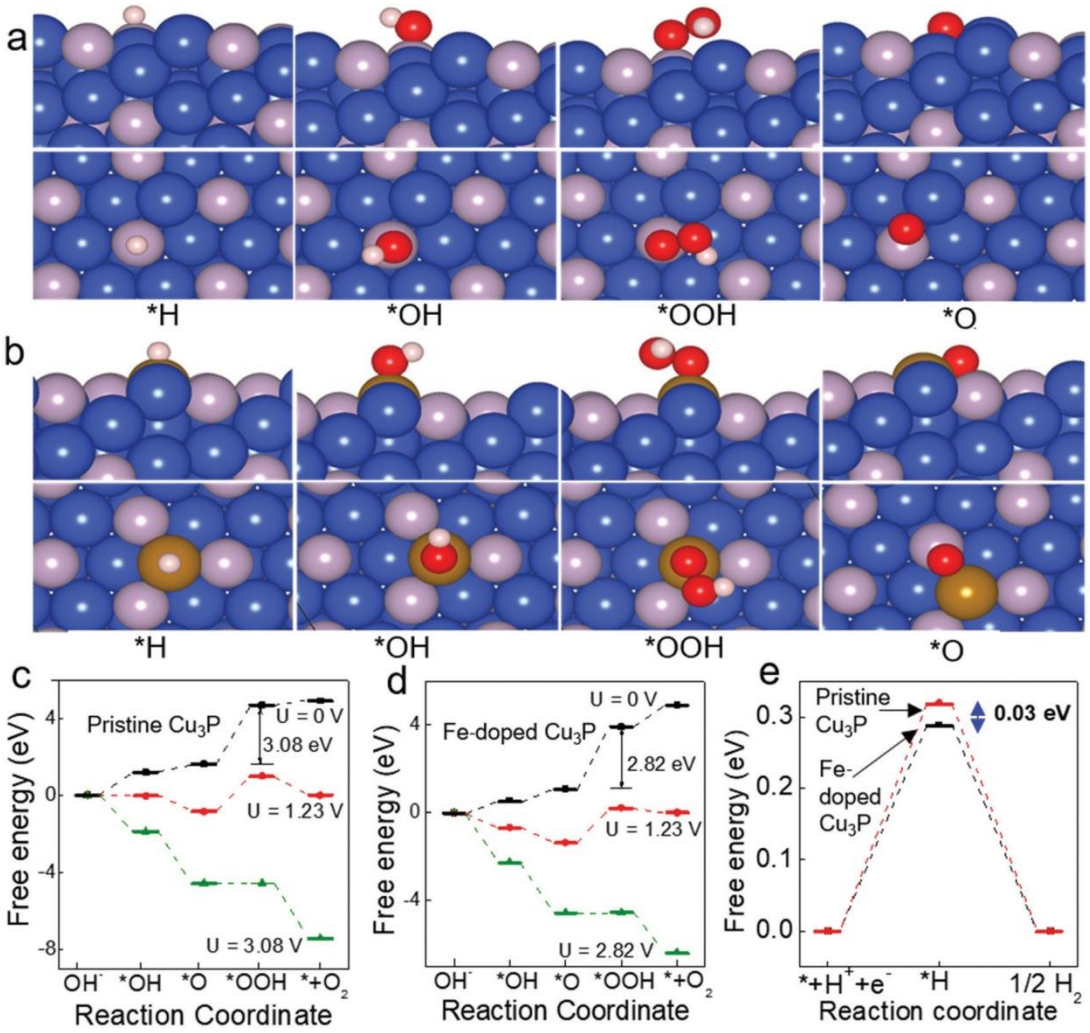

Fig. 4 Adsorption behavior on the surface of (a) pristine and (b) Fe-doped Cu_3P. Free energy diagram of OER on (c) pristine and (d) Fe-doped Cu_3P (blue, grey and brown colors represent the Cu, P and Fe atoms, respectively). (e) Free energy diagram of HER on pristine and Fe-doped Cu_3P.

Table 1 Adsorption energies (eV) of the reaction intermediates on themost preferred sites

Reaction intermediates	Pristine Cu_3P	Fe-doped Cu_3P
*O	−4.40	−4.89
*OH	−2.39	−3.02
*OOH	−3.13	−3.93
*H	−2.18	−2.23
$*H_2O$	−0.26	−0.75

*Sign denotes the adsorbed state.

The reaction free energy (ΔG) associated with all these reaction steps is calculated using eqn (5):[51]

$$\Delta G = \Delta E + \Delta \mathrm{ZPE} - T\Delta S + \Delta G_{\mathrm{U}} + \Delta G_{\mathrm{pH}}, \quad (5)$$

where ΔE, ΔZPE, and ΔS are the difference in total energy, zero-point energy, and entropy, respectively. Here, $\Delta G_{\mathrm{U}} = -eU$, where U is the applied potential and e is the number of transferred electrons. ΔG_{pH} is the correction of the H^+ free energy and depends on whether the reaction under consideration is alkaline or acidic (see the ESI† for computational details).

Fig. 4c and d show the reaction free energy profile for the OER on Cu_3P and Fe-doped Cu_3P, respectively, in the presence/absence of applied electrode potentials. At $U = 0$, all the steps are endergonic on both the catalysts' surfaces. Among the elementary steps, *OOH formation is the rate-limiting step. At equilibrium potential (U = 1.23 V), all the elementary steps except the *OOH formation step are exergonic on both the catalysts. However, all the elementary steps become exergonic on Cu_3P and Fe-doped Cu_3P at the potential 3.08 and 2.82 V, respectively. Therefore, the OP is significantly reduced (by 0.26 V) on the Fe-doped system.

We have also studied the free energy profile for the HER, considering the possible HER mechanism in the alkaline medium [eqn (6) and (7)].[52,53] This reaction in alkaline media requires the first step of water dissociation. In the second step, the adsorbed hydrogen atom combines with an electron transferred from the catalyst surface and a proton from the electrolyte to form one hydrogen molecule. The elementary reactions are as follows [eqn (6) and (7)]:

$$H_2O(l) + e^- + * \rightarrow *H + OH^-, \quad (6)$$

$$H_2O(l) + e^- + *H \rightarrow H_2(g) + OH^- \quad (7)$$

The Gibbs free energy of the adsorbed H* is commonly used to evaluate the HER activity of catalysts,[54] and we find that the Gibbs free energy for H adsorption (Fig. 4e) is 0.32 and 0.29 eV on the surface of Cu_3P and Fe-doped Cu_3P, respectively. It is worth noting that the HER in alkaline media requires an additional first step of water dissociation.[55,56] Therefore, we have calculated the adsorption energy of a H_2O molecule on both the Cu_3P and Fe-doped surfaces. We find that H_2O is strongly adsorbed in both these surfaces, showing the adsorption energy value of −0.26 and −0.75 eV on Cu_3P and Fe-doped Cu_3P surfaces. Therefore, considering both the water adsorption strength and H-adsorption free energy, Fe-doped Cu_3P appears to be a more active catalyst than pristine Cu_3P for the HER in alkaline medium.

Finally, the overall water splitting reaction was performed using $Cu_{2.75}Fe_{0.25}P$ both as the anode and the cathode catalyst in an assembled water electrolyzer system. The reference catalysts IrO_2 and Pt/C loaded on a carbon cloth were used as an anode and a cathode, respectively, for comparison. As shown in the anodic polarization curve, the as-prepared catalysts exhibited high unsaturated current and achieved a current density of 100 mA cm^{-2} at a cell potential of 1.85 V, which is 110 mV larger than the benchmark catalyst (Fig. 5a). The performance, based on current results, is compared with the other non-noble-metal-based bifunctional electrocatalysts (Table S5†). For the stability test, the cyclic voltammogram for the anodic current was collected after 500 cycles, and was close to the initial value exhibited for the two-electrode ($Cu_{2.75}Fe_{0.25}P$||$Cu_{2.75}Fe_{0.25}P$) OER process (Fig. 5b). In addition, the overall water splitting performance was measured under a constant potential (1.8 V) and showed a stable output current up to 32 hours (Fig. 5c). The generation of the H_2 and O_2 gases under the same conditions was shown by recording a movie (see the ESI video†). The H_2 and O_2 gas evolution can be observed at the right and left side electrodes in the movie provided in the supplementary material. For the quantification of H_2 and O_2 gases evolved during the overall water splitting, the faradaic efficiency was measured under a controlled

potential electrolysis for 60 min. As shown in Fig. 5d, the actual detected H_2 and O_2 volume along the reaction time fit well with the volume calculated from the charge transfer, indicating a near-100% faradaic efficiency.

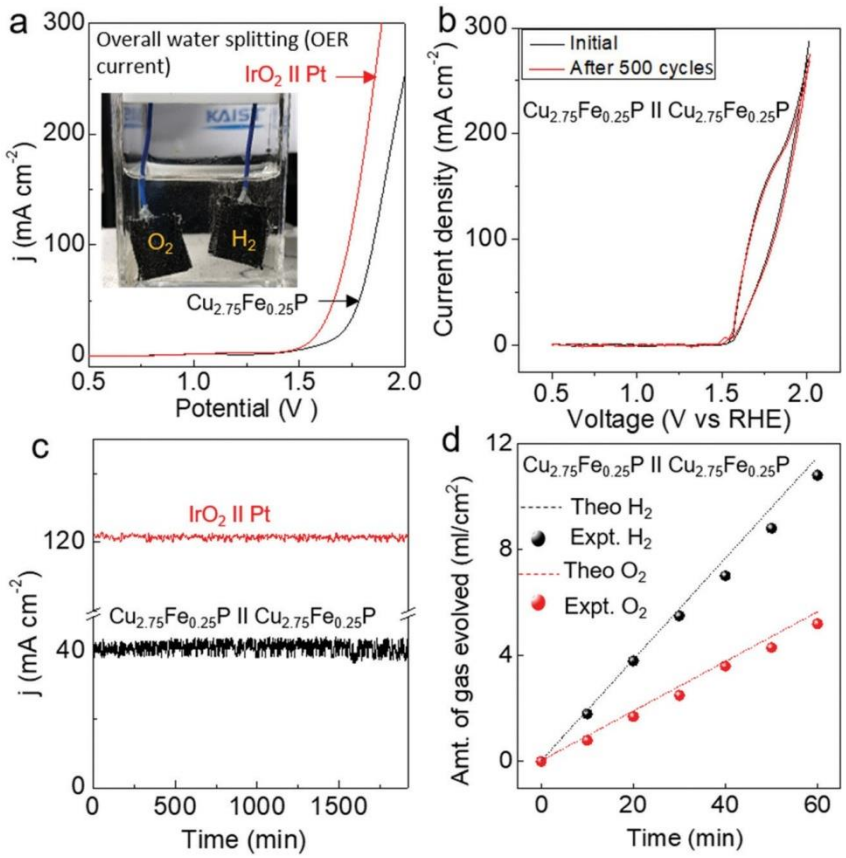

Fig. 5 (a) Anodic polarization curve for the overall water splitting using Fe-doped Cu_3P ($Cu_{2.75}Fe_{0.25}P$); the activity was compared with the commer- cial IrO_2 and Pt/C on a carbon cloth as the anode and cathode (the inset shows the gas bubble generated in the overall water splitting). (b) CV curve of the anodic current for Fe-doped Cu_3P ($Cu_{2.75}Fe_{0.25}P$) after 500 cycles, (c) chronoamperometric test for the anode catalysts at a constant potential of 1.75 V (cell voltage), and (d) temporal plot for the amount of H_2 and O_2 gases evolved during the chronoamperometric run at 2.0 V (cell voltage).

2.3 Post *operando* analysis

In order to understand the structural transformation and active sites during electrochemical operations, post-*operando* microscopic and spectroscopic analyses were carried out for $Cu_{2.75}Fe_{0.25}P$. The post-OER catalyst exhibits a distinct layer on the main catalyst surface (Fig. 6a and b). The newly formed species had low crystallinity and were mainly composed of Cu^{2+} species. The XRD pattern confirms the presence of majorly $Cu(OH)_x$ along with a smaller amount of CuO (Fig. 6f). After the reaction, the deconvoluted Cu $2p_{3/2}$ profile clearly reveals that the $Cu^{\delta+}/Cu^{2+}$ peak intensity ratio decreased as compared to the pre-reaction catalyst (Fig. 6g). The results indicate that, during OER, Cu^0 could transform into meta-stable Cu^{III} species as an active site, which eventually forms air-stable and detectable CuO and $Cu(OH)_x$ phases.[57] We also observed notable changes in the Fe 2p profile after the OER, presumably due to the formation of Fe^{3+}*via* the iron oxyhydroxide species (FeO_xH_y) (Fig. 6h).[58] It is worth noting here that, in anode, Fe could exist in different virtual oxidation states higher than +4,[59] but was not able to directly take part in the OER. The change of the oxidation state of Fe can provide electronic assistance and stability to

the host metal (here Cu) active sites.[60] Nevertheless, the contribution of P atoms cannot be avoided in the OER, because some reaction intermediates, in particular, OH* has a better adsorption stability on the P atoms and Cu–P bonds, as compared to only Cu atoms. The intense peak for P–O species in the XPS profile of post-OER catalyst may be an indication of this. On the other hand, after the HER, the integrated topology of the $Cu_{2.75}Fe_{0.25}P$ catalyst did not change (Fig. 6c). However, the TEM images showed newly segregated particles (approximately 10 nm) with different thicknesses on Cu_3P (Fig. 6d). Evidently, no Cu^{2+} species was detected in either XRD or XPS in the post-HER catalysts. It is suggested that under ambient conditions, metal phosphide nanoparticles are usually oxidized on their surface. In alkaline medium, without any applied potential, the polyphosphate anions on the nanoparticle surface are replaced by hydroxide ions to provide a hydroxide-dominant surface. In the cathode, both the oxidized P and metal species are electrochemically reduced, while the polyphosphate species are simultaneously dissolved in the electrolyte, resulting in a metal-rich phosphide surface. Whereas, in the anode, the sub-surface or even the inner species of metal phosphide nanoparticles are electrochemically oxidized, and the generated polyphosphate species continuously leach into the electrolyte, leading to a relatively thick hydroxide/oxide layer.[61] This has been further supported by the systematic SEM EDXS analysis of cathode and anode after being involved in the bifunctional water splitting activity under different chronoamperometric conditions at the applied potential of 0.5, 1.5 and 2.5 V (Fig. 6e). For the anode catalysts, the relative intensity of oxygen peak increased while the phosporus peak reduced after formation of oxide surface on the pre-catalyst surface. However, the cathode catalyst did not show any such notable changes in their elemental composition. A minor change could be due to the *in situ* formed segregated species (CuP_2 or Cu), but the pre-HER catalyst phase is majorly unchanged. While concluding on the role of metal sites, metallic Cu (Cu^0 nanoparticle) has two advantages, which are (i) negative value for the hydrogen binding energy that facilitates the coupling of hydride ions and (ii) high affinity for adsorbing $^{\cdot}OH$, which is sufficient to facilitate the HER activity in an alkaline medium. Fe doping electronically assisted the stimulation of the metal-rich phase and created a distinct strong adsorption–desorption center for H and OH, which caused the (i) asymmetrical destabilization of the bonds in the water molecule[62] and (ii) stabilization of the O 2p conduction band edge; these appear to provide beneficial properties for hybrid catalysts for bifunctional water splitting.[63]

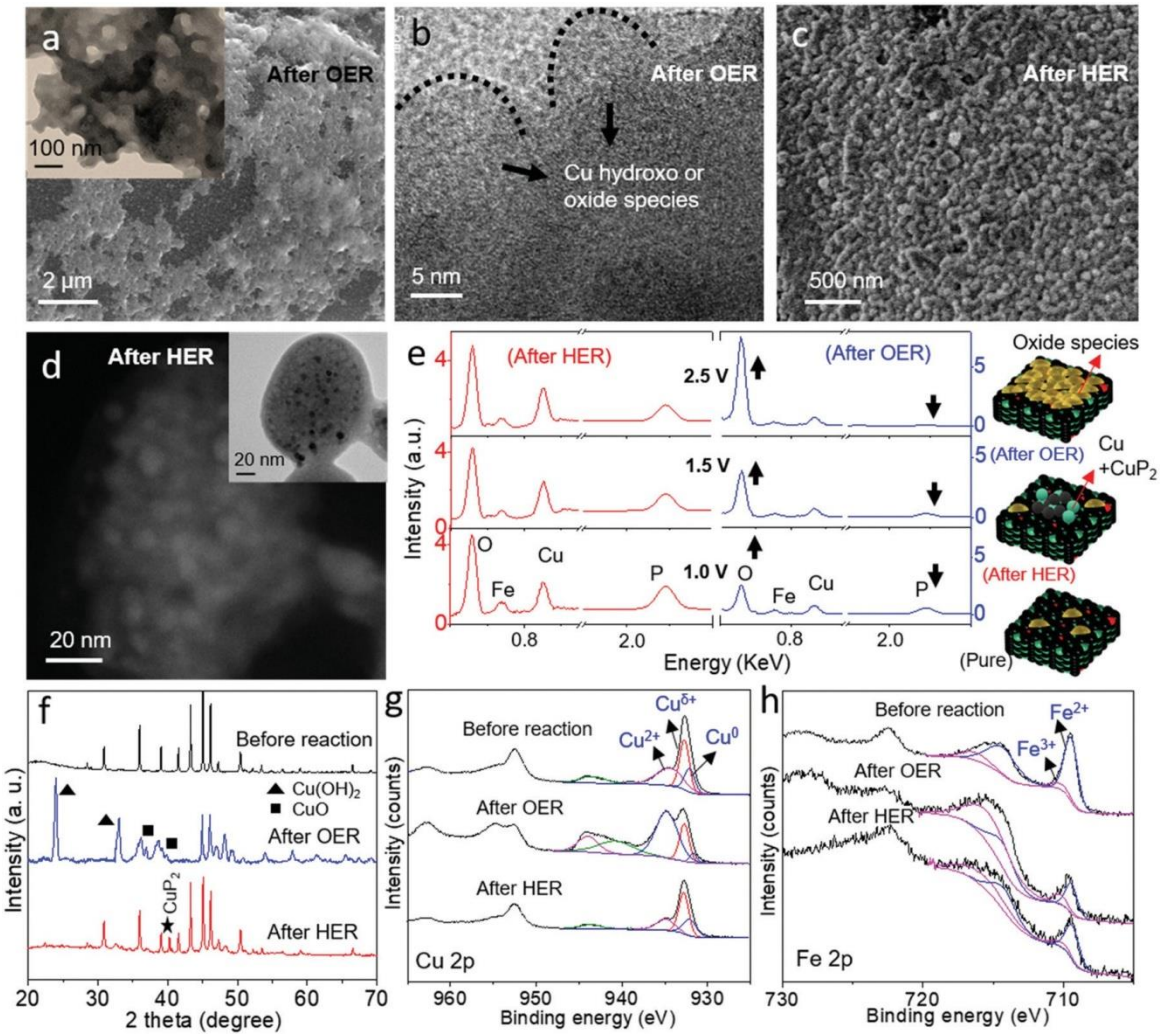

Fig. 6 (a) Post-OER SEM image (the inset shows the TEM image of the same catalyst) and (b) HRTEM of the Fe-doped Cu_3P surface ($Cu_{2.75}Fe_{0.25}P$); (c) post-HER SEM and (d) TEM HADDF of the (the inset shows the bright-field TEM image of the same catalyst) Fe-doped Cu_3P surface ($Cu_{2.75}Fe_{0.25}P$); (e) Large area SEM EDXS of Fe-doped Cu_3P ($Cu_{2.75}Fe_{0.25}P$)/CC electrode used as cathode and anode during the overall water splitting at various applied voltages (1, 1.5 and 2.5 V); the chronoamperometric run was carried out for 15 minutes; the fate of the post-reaction catalyst surface was pictorially demonstrated, where Cu, Fe and P are represented with green, red and black spheres, respectively; (f) wide-angle powder XRD pattern of the post-reaction Fe-doped Cu_3P ($Cu_{2.75}Fe_{0.25}P$); (g) Cu 2p and (h) Fe 2p XPS spectra of Fe-doped Cu_3P ($Cu_{2.75}Fe_{0.25}P$) recorded before and after the electrochemical reaction.

3. Conclusion

In conclusion, we have developed a facile and flexible synthetic approach to grow a series of Fe-doped Cu/Cu_3P nanoparticulate films over 3D electrodes. The Fe-doped Cu/Cu_3P catalysts grown on a carbon cloth paper exhibit excellent bifunctional activity for OER and HER. Fe doping modulates both the electronic structure and the micromorphology of the catalyst, resulting in enhanced HER and OER in a synergistic way. At an optimized Fe doping level ($Cu_{2.75}Fe_{0.25}P$), the overpotential was reduced by 240 and 158 mV for OER and HER, respectively, as compared to the undoped catalyst at 100 mA cm^{-2}. When used for overall water splitting, the $Cu_{2.75}Fe_{0.25}P$/CC electrode couple required an extra cell voltage of 120 mV to achieve the current densities of 100 mA cm^{-2}, compared to the benchmark electrode couple composed of Pt/C and IrO_2. DFT calculations indicate that Fe-doping alters the surface active sites towards Fe-center from the P-center

which is primary in the pristine Cu_3P catalyst, and reduced the reaction overpotential in Fe-doped system as compared to undoped catalyst. Post-*operando* studies clearly reveal the surface active species (oxide and hydroxide for the anode and metal and metal phosphide for the cathode) that took part in stabilizing and destabilizing the reaction intermediates, thus supporting the underlying mechanism behind alkaline water electrolysis. This work can provide a route map for further tuning the doped metal@metal phosphide pre-catalysts for efficient bifunctional electrocatalysis in alkaline media.

4. Experimental section

4.1 Material synthesis

Carbon cloth (CC) was cut into 2 × 3 cm pieces and cleaned by sonication in DI water, followed by ethanol for 30 min prior to using it as a substrate. In the three separate sets of reaction batches, 236.7, 217.4, and 193.3 mg of $Cu(NO_3)_2{\cdot}3H_2O$ was taken with 2.6 (2 mol%), 12.7 (10 mol%) and 25.3 mg (20 mol%) of $FeCl_2$, respectively, and dissolved in 20 mL of water. 300 mg of urea and 40 mg of NH_4F were added to the resulting mixture and stirred for 30 min to prepare a homogeneous solution, and then poured into a 25 ml Teflon-lined solvothermal container. The clean carbon cloth was immersed in the resultant solution, and this reaction system was kept at 150 °C for 18 h. After natural cooling, the as-obtained $CuFe(OH)_x$ was washed with water three times and dried at 60 °C. To synthesize Fe-doped Cu_3P, the dried $CuFe(OH)_x$/CF was placed in the upstream side of a horizontal tube furnace. 500 mg of NaH_2PO_2 was placed 4 cm away from CC/$CuFe(OH)_x$, toward the side of the gas flow. Finally, it was heated at 300 °C for 2 h in a constant flow of Ar (50 ml min^{-1}) at a heating rate of 2 °C min^{-1}. To prepare the undoped Cu_3P/CC, only 241.6 mg of $Cu(NO_3)_2{\cdot}3H_2O$ was taken during the hydrothermal treatment. The subsequent procedure followed is similar to that for Fe-doped Cu_3P. Commercial Pt/C and IrO_2 were used to prepare the catalyst inks for the Pt/C/CC and IrO_2/CC electrodes. The catalyst inks were prepared by mixing 5 mg of the catalyst with 20 µl of 5 wt% Nafion solution and 4 ml of isopropyl alcohol (99.7%, Merck).

4.2 Electrochemical analysis

All electrochemical measurements were performed using a multichannel potentiostat (VersaStat3, Princeton Applied Research, USA) electrochemical workstation at room temperature. The catalysts were evaluated in 1 M KOH aqueous solution using a conventional three-electrode configuration, in which $Cu_{3-x}Fe_xP$/CF was used as the working electrode, platinum wire as the counter electrode, and Hg/HgO (saturated KOH) electrode as the reference electrode. Linear sweep voltammetry (LSV) polarization curves were recorded at a scan rate of 20 mV s^{-1} without iR compensation. Chronopotentiometry (CP) curves was recorded at a constant potential mentioned with the plot. The electrochemical surface area (ECSA) was evaluated by the capacitance measurements in the non-faradaic potential region at various scan rates of 20, 30, 40, 50, 60, 80 and, 100 mV S^{-1}. The overall water splitting measurements were performed using $Cu_{2.75}Fe_{0.25}P$/CF as both the anode and cathode in a two-electrode configuration. The active geometric area of both electrodes was 1 × 1 cm. The mass of the catalyst was approximately 2 mg cm^{-2}. All potentials in this work were reported with respect to RHE, which were converted according to the following equation:

$$E\ (RHE) = E\ (Hg/HgO) + 0.098 + 0.059\ pH.$$

A sealed H-cell electrochemical reactor was taken and filled with electrolyte above the connecting bridge to isolate and measure the amount of gas evolved during the overall water splitting. The reactor was connected online with GC equipped with an isocratic pump and thermal conductivity detector. The automatic sampling method was used to inject headspace gases with 10 min of interval in a cyclic manner.

The evolved H_2 and O_2 gases were emitted at a retention time of 1 and 1.5 min. The H_2 and O_2 gas evolution can be observed at the right and left side electrodes in the movie provided in the supplementary material.

Conflicts of interest

There are no conflicts to declare.

Acknowledgements

I.M. and J.Y.P. acknowledge the support from the Institute for Basic Science (IBS) [IBS-R004]. A.M. and F.D.A. received funding from the European Union's Horizon 2020 Framework Programme research and innovation programme under the Grant Agreement no. 764047 of the ESPRESSO project. The Ministero dell'Istruzione, dell'Università e della Ricerca (MIUR) and the University of Perugia are acknowledged for the financial support through the program “Dipartimenti di Eccellenza 2018–2022” (Grant AMIS) to F.D.A.

References

1. N. S. Lewis and D. G. Nocera , *Proc. Natl. Acad. Sci. U. S. A.*, 2006, **103** , 15729 —15735
2. D. G. Nocera *Acc. Chem. Res.*, 2012, **45** , 767 —776
3. Z. W. She , J. Kibsgaard , C. F. Dickens , I. Chorkendorff , J. K. Nørskov and T. F. Jaramillo , *Science*, 2017, **55** , eaad4998
4. M. Huynh , T. Ozel , C. Liu , E. C. Lau and D. G. Nocera , *Chem. Sci.*, 2017, **8** , 4779 —4794
5. I. Mondal , S. Y. Moon , H. Kim and J. Y. Park , *Int. J. Hydrogen Energy*, 2019, **44** , 7241 —7251
6. E. J. Popczun , J. R. McKone , C. G. Read , A. J. Biacchi , A. M. Wiltrout , S. Lewis and R. E. Schaak , *J. Am. Chem. Soc.*, 2013, **135** , 9267 —9270
7. J. Tian , Q. Liu , A. M. Asiri and X. Sun , *J. Am. Chem. Soc.*, 2014, **136** , 7587 —7590
8. J. Tian , Q. Liu , N. Cheng , A. M. Asiri and X. Sun , *Angew. Chem., Int. Ed.*, 2014, **53** , 9577 —9581
9. L. Yu , J. Zhang , Y. Dang , J. He , Z. Tobin , P. Kerns , Y. Dou , Y. Jiang , Y. He and S. L. Suib , *ACS Catal.*, 2019, **9** , 6919 —6928
10. I. Mondal , H. Lee , H. Kim and J. Y. Park , *Adv. Funct. Mater.*, 2020, **30** , 1908239
11. S. Yao , V. Forstner , P. W. Menezes , C. Panda , S. Mebs , E. M. Zolnhofer , M. E. Miehlich , T. Szilvási , N. A. Kumar , M. Haumann , K. Meyer , H. Grützmacher and M. Driess , *Chem. Sci.*, 2018, **9** , 8590 —8597
12. W. Xiao , L. Zhang , D. Bukhvalov , Z. Chen , Z. Zou , L. Shang , X. Yang , D. Yan , F. Han and T. Zhang , *Nano Energy*, 2020, **70** , 104445
13. K. Xu , H. Ding , H. Lv , P. Chen , X. Lu , H. Cheng , T. Zhou , S. Liu , X. Wu , C. Wu and Y. Xie , *Adv. Mater.*, 2016, **28** , 3326 —3332
14. L.-L. Feng , G. Yu , Y. Wu , G.-D. Li , H. Li , Y. Sun , T. Asefa , W. Chen and X. J. Zou , *J. Am. Chem. Soc.*, 2015, **137** , 14023 —14026

15. J.-Y. Wang , T. Ouyang , N. Li , T. Ma and Z.-Q. Liu , *Sci. Bull.*, 2018, **63** , 1130 —1140

16. S. Kalra , R. Beltrán-Suito , C. Das , T. Hellmann , P. W. Menezes and M. Driess , *Chem. – Asian J.*, 2020, **15** , 852 —859

17. B. Chakraborty , R. Beltrán-Suito , V. Hlukhyy , J. Schmidt , P. W. Menezes and M. Driess , *ChemSusChem*, 2020, **13** , 3222 —3229

18. I. Mondal , S. Y. Moon , H. Lee , H. Kim and J. Y. Park , *J. Mater. Chem. A*, 2019, **7** , 19258 —19268

19. F. Yu , H. Zhou , Z. Zhu , J. Sun , R. He , J. Bao , S. Chen and Z. Ren , *ACS Catal.*, 2017, **7** , 2052 —2057

20. J. Xu , J. Li , D. Xiong , B. Zhang , Y. Liu , K.-H. Wu , I. Amorim , W. Li and L. Liu , *Chem. Sci.*, 2018, **9** , 3470 —3476

21. X. Xiao , C.-T. He , S. Zhao , J. Li , W. Lin , Z. Yuan , Q. Zhang , S. Wang , L. Dai and D. A. Yu , *Energy Environ. Sci.*, 2017, **10** , 893 —899

22. X. Jia , X. Zhang , J. Zhao , Y. Zhao , Y. Zhao , G. I. N. Waterhouse , R. Shi , L. Z. Wu , C. H. Tung and T. Zhang , *J. Energy Chem.*, 2019, **34** , 57 —63

23. A. Dutta , S. Mutyala , A. K. Samantara , S. Beram , B. K. Jena and N. Pradhan , *ACS Energy Lett.*, 2018, **3** , 141 —148

24. A. Dutta and N. Pradhan , *J. Phys. Chem. Lett.*, 2017, **8** , 144 —152

25. S. Jin *ACS Energy Lett.*, 2017, **2** , 1937 —1938

26. X. Xiao , L. Tao , M. Li , X. Lv , D. Huang , X. Jiang , H. Pan , M. Wang and Y. Shen , *Chem. Sci.*, 2018, **9** , 1970 —1975

27. G.-A. Li , C.-Y. Wang , W.-C. Chang and H.-Y. Tuan , *ACS Nano*, 2016, **10** , 8632 —8640

28. L. De Trizio , A. Figuerola , L. Manna , A. Genovese , C. George , R. Brescia , Z. Saghi , R. Simonutti , M. Van Huis and A. Falqui , *ACS Nano*, 2012, **6** , 32 —41

29. X. He , R. Wang , M. C. Stan , E. Paillard , J. Wang , H. Frielinghaus and J. Li , *Adv. Mater. Interfaces*, 2017, **4** , 1601047

30. M. C. Stan , R. Klöpsch , A. Bhaskar , J. Li , S. Passerini and M. Winter , *Adv. Energy Mater.*, 2013, **3** , 231 —238

31. L. De Trizio , F. De Donato , A. Casu , A. Genovese , A. Falqui , M. Povia and L. Manna , *ACS Nano*, 2013, **7** , 3997 —4005

32. A. Dutta , S. K. Dutta , S. K. Mehetor , I. Mondal , U. Pal and N. Pradhan , *Chem. Mater.*, 2016, **28** , 1872 —1878

33. L. Wei , K. Goh , Ö. Birer , H. E. Karahan , J. Chang , S. Zhai , X. Chen and Y. Chen , *Nanoscale*, 2017, **9** , 4401 —4408

34. S. Wei , K. Qi , Z. Jin , J. Cao , W. Zheng , H. Chen and X. Cui , *ACS Omega*, 2016, **1** , 1367 —1373

35. N. Li , D. Kwabena Bediako , R. G. Hadt , D. Hayes , T. J. Kempa , F. von Cube , D. C. Bell , L. X. Chen and D. G. Nocera , *Proc. Natl. Acad. Sci. U. S. A.*, 2017, **114** , 1486 —1149

36. M. Sieberer , J. Redinger and P. Mohn , *Phys. Rev. B: Condens. Matter Mater. Phys.*, 2007, **75** , 035203

37. Y.-C. Chen , Z.-B. Chen , Y.-J. Lin and Y.-K. Hsu , *ACS Sustainable Chem. Eng.*, 2017, **5** , 3863 —3870

38. H. T. Phan and A. J. Haes , *J. Phys. Chem. C*, 2019, **123** , 16495 —16507

39. K. Liu , C. Zhang , Y. Sun , G. Zhang , X. Shen , F. Zou , H. Zhang , Z. Wu , E. C. Wegener , C. J. Taubert , J. T. Miller , Z. Peng and Y. Zhu , *ACS Nano*, 2018, **12** , 158 —167

40. C. Tang , L. F. Gan , R. Zhang , W. B. Lu , X. E. Jiang , A. M. Asiri , X. P. Sun , J. Wang and L. Chen , *Nano Lett.*, 2017, **16** , 6617 —6621

41. T. Shinagawa , A. T. Garcia-Esparza and K. Takanabe , *Sci. Rep.*, 2015, **5** , 13801

42. F. Yu , H. Q. Zhou , Y. F. Huang , J. Y. Sun , F. Qin , J. M. Bao , W. A. Goddardiii , S. Chen and Z. F. Ren , *Nat. Commun.*, 2018, **9** , 2551

43. J. E. Thorne , J.-W. Jang , E. Y. Liu and D. Wang , *Chem. Sci.*, 2016, **7** , 3347 —3354.

44. Y. Yoon , B. Yan and Y. Surendranath , *J. Am. Chem. Soc.*, 2018, **140** , 2397 —2400

45. C. Hu , L. Zhang and J. Gong , *Energy Environ. Sci.*, 2019, **12** , 2620 —2645

46. C. Panda , P. W. Menezes , M. Z. S. Orthmann and M. Driess , *ACS Energy Lett.*, 2019, **4** , 747 —754

47. D. Friebel , M. W. Louie , M. Bajdich , K. E. Sanwald , Y. Cai , A. M. Wise , M. J. Cheng , D. Sokaras , T.-C. Weng , R. Alonso-Mori , R. C. Davis , J. R. Bargar , J. K. Nörskov , A. Nilsson and A. T. Bell , *J. Am. Chem. Soc.*, 2015, **137** , 1305 —1313

48. J. P. Xiao , A. Kuc , T. Frauenheim and T. Heine , *Phys. Rev. Lett.*, 2014, **112** , 106102

49. J. Rossmeisl , A. Logadottir and J. K. Nørskov , *Chem. Phys.*, 2005, **319** , 178 —184

50. J. Rossmeisl , Z. W. Qu , H. Zhu , G. J. Kroes and J. K. Nørskov , *J. Electroanal. Chem.*, 2007, **607** , 83 —89

51. E. Skúlason , V. Tripkovic , M. E. Björketun , S. Gudmundsdóttir , G. Karlberg , J. Rossmeisl , T. Bligaard , H. Jónsson and J. K. Nørskov , *J. Phys. Chem. C*, 2010, **114** , 18182 —18197

52. I. Mondal , M. Srikanth , K. Srinivasu , Y. Soujanya and U. Pal , *J. Phys. Chem. C*, 2017, **121** , 2597 —2604

53. J. Yang , Y. Ji , Q. Shao , N. Zhang , Y. Li and X. Huan , *Adv. Funct. Mater.*, 2018, **28** , 1803722

54. J. Greeley , T. F. Jaramillo , J. Bonde , I. Chorkendorff and J. K. Nørskov , *Nat. Mater.*, 2006, **5** , 909 —913

55. H. Liang , A. N. Gandi , D. H. Anjum , X. Wang , U. Schwingenschlogl and H. N. Alshareef , *Nano Lett.*, 2016, **16** , 7718 —7725

56. H. Xu , D. Chen , D. Cao and X. C. Zeng , *Nat. Catal.*, 2018, **1** , 339 —348

57. Y. Deng , A. D. Handoko , Y. Du , S. Xi and B. S. Yeo , *ACS Catal.*, 2016, **6** , 2473 —2481

58. H. Ali-Löytty , M. W. Louie , M. R. Singh , L. Li , H. G. Sanchez Casalongue , H. Ogasawara , E. J. Crumlin , Z. Liu , A. T. Bell , A. Nilsson and D. Friebel , *J. Phys. Chem. C*, 2016, **120** , 2247 —2253

59. S. Licht , B. Wang and S. Ghosh , *Science*, 1999, **285** , 1039 —1042

60. J. Y. Chen , L. Dang , H. Liang , W. Bi , J. B. Gerken , S. Jin , E. E. Alp and S. S. Stahl , *J. Am. Chem. Soc.*, 2015, **137** , 15090 —15093

61. Z. Wu , Q. Gan , X. Li , Y. Zhong and H. Wang , *J. Phys. Chem. C*, 2018, **122** , 2848 —2853

62. C. T. Dinh , A. Jain , F. P. G. de Arquer , P. D. Luna , J. Li , N. Wang , X. Zheng , J. Cai , B. Z. Gregory , O. Voznyy , B. Zhang , M. Liu , D. Sinton , E. J. Crumlin and E. H. Sargent , *Nat. Energy*, 2019, **4** , 107

63. F. Massel , S. Ahmadi , M. Hahlin , Y. S. Liu , J. H. Guo , T. Edvinsson , H. Rensmo and L.-C. Duda , *J. Electron Spectrosc. Relat. Phenom.*, 2018, **224** , 3 —7

Footnote

1. † Electronic supplementary information (ESI) available. See DOI: 10.1039/d0nr03414b